Supporting Information

Low-Work-Function Metals Boost Selective and Fast Scission of Methanol C−H Bond

Nengchao Luo,[1,†] Wei Nie,[1,2,†] Junju Mu,[1,†] Shiyang Liu,[1,2] Mingrun Li,[1] Jian Zhang,[1] Zhuyan Gao,[1,2] Fengtao Fan,[1] Feng Wang[1,*]

[1] State Key Laboratory of Catalysis, Dalian National Laboratory for Clean Energy, Dalian Institute of Chemical Physics, Chinese Academy of Sciences, Dalian 116023, P. R. China

[2] University of Chinese Academy of Sciences, Beijing 100049, P. R. China

Corresponding author:

*Feng Wang: wangfeng@dicp.ac.cn

† These authors contribute equally to this work.

Content

Experimental procedures

Materials. MeOH (99.9%), $ZnSO_4 \cdot 7H_2O$ (99.5%), $InCl_3 \cdot 4H_2O$ (99.9%), thioacetamide (TAA, 99%), diethylene glycol (99+%), $NaBH_4$ (98%), 2,4-dinitrophenylhydrazine (DNPH, 98+%), *p*-chloroanisole (99%) and SiO_2 (30 nm, hydrophilic) were purchased from Shanghai Aladdin Bio-Chem Technology Co. Ltd. 1,3-propanediol (98%) and disodium citrate hydrate (99%) were purchased from TCI Shanghai and Sigma Aldrich, respectively. All the reagents were used as received without further purification.

Preparation of catalysts

Preparation of ZnS and In_2S_3 catalysts. ZnS and In_2S_3 were prepared by similar solvothermal method. Take ZnS as an example. Typically, $ZnSO_4 \cdot 7H_2O$ (4.0 mmol, 1150.2 mg) and NaCl (194.9 mg) were dissolved in 30 ml of absolute ethanol in a 100 ml conical flask and magnetically stirred for 30 min at room temperature. TAA (599.9 mg) was then added to the above solution. After being stirred for another 30 min, the mixture was transferred to a 50-ml stainless Teflon-lined autoclave, tightly sealed and placed in a 160 °C oven for 20 h. The autoclave was then naturally cooled to room temperature. After being washed with absolute ethanol (3 × 25 ml), deionized water (2 × 25 ml) and again absolute ethanol (25 ml), a yellow solid was obtained after being dried in vacuum at 60 °C for 12 h. For the preparation of In_2S_3, 2.67 mmol of $InCl_3 \cdot 4H_2O$ (781.8 mg) and 217.2 mg of NaCl were used.

Preparation of ball-milled $ZnIn_2S_4$. Ball-milled $ZnIn_2S_4$ is well dispersed and used for KPFM measurement. Typically, 500 mg of $ZnIn_2S_4$ and agate balls (about 42 mg) were added into the Teflon-lined metal can. Before being tightly sealed, the atmosphere of the metal can was replaced to Ar. The metal can was then installed in ball mill machine and underwent ball-milling for 8 min at a rate of 400 rpm. The obtained ball-milled $ZnIn_2S_4$ was dispersed in 20 ml of methanol for further use.

Preparation of metallic In nanoparticles (In^0 NPs), Cd^0 NPs and Bi^0 NPs. In^0 NPs were prepared by citrate-assisted reduction by $NaBH_4$ according to the literature.[1] Briefly, $InCl_3 \cdot 4H_2O$ (1.25 mmol, 362.5 mg) and disodium citrate hydrate (0.95 mmol, 250.0 mg) were filled into a three-necked flask together with 50.0 ml of diethylene glycol. Under dynamic argon purging and vigorous stirring, the solution was heated to 100 °C in an oil bath. Afterwards, $NaBH_4$ (12.5 mmol, 472.5 mg, In^{3+}:BH_4^- = 1:10) that was dissolved in 1.0 ml of deionized

water was rapidly injected to the colorless transparent diethylene glycol solution, the solution changed its color to dark brown in seconds. The solution was remained at 100 °C for 1 min, and then naturally cooled to room temperature under dynamic argon purging. After centrifugation at 2000 rpm for 10 min to remove the precipitate, the In^0 NPs with size of *c.a.* 8 nm were obtained and stored in diethylene glycol solution. To obtain In^0 NPs with size of *c.a.* 100 nm, 2.5 mmol of $NaNH_4$ (95 mg, In^{3+}:BH_4^- = 1:2) dissolved in 1.0 ml of deionized water was rapidly injected to diethylene glycol solution. Naturally precipitating for 2 h obtained In^0 NPs with size of *c.a.* 100 nm and dispersed in diethylene glycol solution. Cd^0 NPs and Bi^0 NPs were prepared by a method similar to In^0 NPs except that $Cd(OAc)_2 \cdot 2H_2O$ (1.25 mmol, 333.2 mg) and $Bi(NO_3) \cdot 5H_2O$ (1.25 mmol, 606.3 mg) were used, respectively.

Preparation of In/ZnS, Cd/ZnS and Bi/ZnS. In/ZnS, Cd/ZnS and Bi/ZnS were prepared by in situ photodeposition with the diethylene glycol solution of In^0 NPs, Cd^0 NPs and Bi^0 NPs, respectively, as the precursor. Take In/ZnS as an example, 1.4 ml of MeOH, 25 μl of the as-prepared diethylene glycol solution of In^0 NPs, 75 μl of diethylene glycol and 10 mg of ZnS were added into a quartze tube, of which the atmosphere was replaced by 2 bar of 5 vol% CO/Ar. After tightly sealed, the quartze tube was irradiatd by 18 W LEDs (365 nm) for 6 h. The Cd/ZnS and Bi/ZnS were prepared by a similar method except that Cd^0 NPs and Bi^0 NPs was used, respectively.

Preparation of Pt/P25. Pt/P25 was prepared by impregnation method by using H_2PtCl_6 and Degussa P25, the Pt content was 0.3 wt%. Typically, P25 (500 mg) was dispersed in deionized water (10 ml) with vigorous stirring, and H_2PtCl_6 (1.011 ml, 7.61 mmol l^{-1}) aqueous solution was added dropwise. After stirring for 6 h, the solution was evaporated on a 100 °C hot plate. The grey Pt/P25 was obtained after reducing at 400 °C by H_2 (30 ml min^{-1}) for 2h with a ramp rate of 10 °C min^{-1}.

Preparation of CdS catalyst. CdS was prepared according to a literature.[2] Typically, $Cd(NO_3)_2 \cdot 4H_2O$ (16.2 mmol) and thiourea (48.6 mmol) were dispersed in 80 ml of ethylenediamine in a 130 ml stainless Teflon-lined autoclave. After being stirred for another 30 min, the autoclave was tightly sealed and placed in a 160 °C oven for 24 h. The autoclave was then naturally cooled to room temperature. After being washed with absolute ethanol (3 × 25 ml) and deionized water (3 × 25 ml), a yellow solid was obtained after being dried in vacuum at 60 °C for 12 h.

Quantitative analysis of products

Quantitative analysis of H_2. H_2 was quantified with He as the internal standard. After reactions, He (20.0 mL) was injected into the reaction systems, well mixed and analyzed by GC equipped with thermal conductivity detector (GC-TCD, Techcomp 7900, column: TDX-01) with Ar as the carrier gas. The calibration coefficients between the injected volume of H_2 and He with respect to their TCD response were 0.561 and 1.137, respectively. The produced H_2 can be calculated from the following equation:

$$n(\mathrm{H_2}) = \frac{0.561 \times I(\mathrm{H_2}) \times V(\mathrm{He})/\mathrm{m}\,l}{1.137 \times I(\mathrm{He})} \times \frac{101.3}{8.314 \times 298} mmol = 0.0202 \times \frac{I(\mathrm{H_2})}{I(\mathrm{He})} \times \frac{V(\mathrm{He})}{ml}\, mmol \quad (1)$$

Where $n(\mathrm{H_2})$ is the produced H_2 in the reaction system, mmol; $I(\mathrm{H_2})$ and $I(\mathrm{He})$ are the TCD response of H_2 and He, respectively. $V(\mathrm{He})$ is the injected volume of He. The produced H_2 is then expressed as $n(\mathrm{H_2})/m_{\mathrm{catalyst}}$, here, $m_{catalyst}$ represents the mass of the catalyst.

Quantitative analysis of HCHO. HCHO was quantified by a derivatization method with *p*-chloroanisole as the internal standard. After a typical reaction, an internal methanol solution containing *p*-chloroanisole and 1,3-propanediol was added into the reaction mixture, followed by filtration through a 0.22 μm Nylon syringe filter to remove the catalyst. Samples of the reaction mixture (0.1 μL) were diluted with MeCN for 50 times. Then 1.0 ml of the diluted reaction mixture and 1.0 ml of 2,4-dinitrophenylhydrazine (DNPH)/MeCN solution (0.25 g of DNPH and 2.0 ml of glacial acetic acid were dissolved in MeCN to form a 500-ml solution) were mixed and heated at 45 °C for 60 min to totally convert HCHO into HCHO-DNPH (Figure S15C). The mixture was then analyzed by high performance liquid chromatography (HPLC, waters XSelect HSS-PFP column, maintained at 30 °C, UV-detector at 232 nm, mobile phase: 45% CH_3CN balanced by H_2O, 1.0 ml min^{-1}) after filtration through a 0.22 μm Nylon syringe filter.

Quantitative analysis of EG. EG was quantitatively analyzed with 1,3-propanediol (1,3-PD) as the internal standard. The residual reaction mixture that was partially used for quantifying HCHO was directly analyzed by gas chromatography equipped with a flame ionization detector (GC-FID, Agilent 7890A, column: HP-5, 30 m × 530 μm × 1.5 μm). The productivity and selectivity of HCHO and EG were calculated by the following equations:

$$\text{Productivitity of product} = \frac{n_{\text{product}}}{m_{\text{catalyst}}} \times 100\% \quad (2)$$

$$\text{Selectivity of HCHO} = \frac{n_{\text{HCHO}}}{n_{\text{HCHO}} + 2n_{\text{EG}}} \times 100\% \quad (3)$$

$$\text{Selectivity of EG} = \frac{2n_{\text{EG}}}{n_{\text{HCHO}} + 2n_{\text{EG}}} \times 100\% \quad (4)$$

Where n_{product}, n_{HCHO} and n_{EG} are the moles of generated product, HCHO and EG, respectively.

Apparent quantum yield measurements

The AQYs of EG and H_2 in photocatalytic dehydrocoupling of methanol was measured over ZIS-40 catalyst with Xenon lamp (365 ± 5 nm) by top irradiation. The number of photons reaching the top of the reaction solution was measured by a calibrated Si photodiode (LS-100, EKO Instruments Co., Ltd.). The apparent quantum yields (η) for the formation of EG (η_{EG}) and H_2 (η_{H_2}) were calculated by the following equations:

$$\eta_{\text{EG}} = \frac{2n_{\text{EG}}\,(mol) \times N_{\text{A}}\,(mol^{-1})}{I\,(cm^{-2}\cdot s^{-1}) \times t\ (s) \times S\ (cm^2)} \times 100\% \quad (5)$$

$$\eta_{\text{H}_2} = \frac{2n_{\text{H}_2}\,(mol) \times N_{\text{A}}\,(mol^{-1})}{I\,(cm^{-2}\cdot s^{-1}) \times t\ (s) \times S\ (cm^2)} \times 100\% \quad (6)$$

Where n_{EG}, n_{H_2}, N_{A}, I, t and S represent the produced EG and H_2, Avogadro's constant, light intensity, reaction time and irradiation area, respectively.

General characterizations

Powder X-ray diffraction patterns. XRD was conducted with a PANalytical X-Pert PRO diffractometer, using Cu-Kα radiation at 40 kV and 20 mA. Continuous scans were collected in the 2θ range of 10−80°.

Transmission electron microscopy. Samples for TEM were prepared by dispersing catalyst in methanol and sonication for 20 min. The suspension (15 μl) was loaded onto a Cu TEM grid and dried. TEM images were obtained using a JEOL JEM-2100.

Scanning transmission electron microscopy. Samples for STEM were obtained by the reaction in methanol for 10 h under the irradiation of 18 W LEDs (365 ± 5 nm). STEM and High-resolution transmission electron microscopy (HRTEM) were performed using a JEOL JEM F200 electron microscope operated at 200 kV, equipped with a high-angle annular dark field (HAADF) detector. Compositional maps were obtained with energy-dispersive X-ray spectroscopy (EDS) using dual silicon drift detectors. For EDS analysis, Zn K, In L

and S K peaks were used.

DFT calculations

The Vienna Ab Initio Package (VASP)[3-4] was employed to perform spin-polarized DFT calculations within the generalized gradient approximation (GGA) using the PBE[5] functional formulation. The ionic cores were described by the projected augmented wave (PAW) pseudopotentials[6-7] and valence electrons were explicitly taken into account using a plane-wave basis set with an energy cutoff of 400 eV. Partial occupancies of the Kohn−Sham orbitals were allowed using the Gaussian smearing method with a width of 0.10 eV. The electronic energy was considered self-consistent when the energy change of the whole simulated system was smaller than 10^{-7} eV. Geometry optimization was considered convergent when the energy change was smaller than 10^{-6} eV. Grimme's DFT-D3 methodology[8] was used to describe the dispersion interactions among all the atoms.

The equilibrium lattice constants of bulk $ZnIn_2S_4$ hexagonal unit cell were calculated, when using an 11×11×2 Monkhorst-Pack grid for Brillouin zone sampling, to be $a = b = 3.896$ Å and $c = 24.498$ Å, which agree well with experimental ones.[9] This unit cell was used to construct the (0001) surface with a *p*(4x4) periodicity and 7 atomic layers (S-Zn-S-In-S-In-S) with a 15 Å of vacuum in the c direction between the surface and its periodic images. The In^0 NP used contains 10 indium atoms. A larger control system of the (0001) surface, with a p(5x5) periodicity of the unit cell and a large In0 NP consisting of 20 indium atoms, was constructed to check if any size-effect is involved. For both systems, the Zn side of the layer was considered for C−H and O−H bonds cleavage during the calculations since Zn side (Zn3d + S3s3p) contributed to the valence band maximum of $ZnIn_2S_4$. Bader charge analysis was performed on the all-electron charge density files. The correct valence electron count based on Bader partitioning was achieved using the default grids.

Supplementary Tables

Table S1. Comparison of catalysts for photocatalytic DMEG.[a]

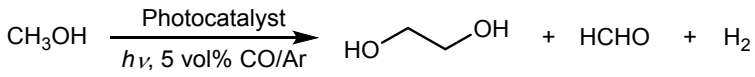

Entry	Catalyst	Productivity (mmol $g_{catalyst}^{-1}$)			Product selectivity (%)		
		HCHO	EG	Others	HCHO	EG	Others
1[b]	$ZnIn_2S_4$	11.9	5.4	0	52	48	0
2	In/$ZnIn_2S_4$	16.1	14.5	0.3	35	63	2
3	In/ZIS	15.3	21.7	1.4	25	68	7
4	In/ZIS-40	16.7	30.1	2.6	20	71	9
5[c]	In/ZIS-40	10.0	29.0	0.4	15	84	1
6[d]	In/ZIS-10	100.4	272.0	11.2	15	80	5
7	ZnS	3.5	1.6	0	52	48	0
8	In_2S_3	0.2	0	0	100	0	0
9	Pt/$ZnIn_2S_4$-2.0 wt%	29.9	0	0	100	0	0
10	CdS nanorods	0.1	0	0	100	0	0
11	Pt/P25-0.3 wt%	63.9	0	0	100	0	0

[a] Standard reaction conditions: 1.5 ml of MeOH, 10 mg of catalyst, 2 bar of 5 vol% CO/Ar, 18 W LEDs (365 nm), 6 h. [b] Reaction under Ar atmosphere. [c] 50 ml of MeOH, 100 mg of ZIS-40, 103 W LEDs (365 ± 10 nm, light intensity at the center was 14.3 mW cm^{-2}). [d] Productivity based on ZIS. The reactions were conducted twice.

Table S2. Measured apparent quantum yields of HCHO, EG and their sum.

	HCHO	EG	HCHO + EG
AQY-1st	11.6	16.4	28.0
AQY-2nd	11.1	14.9	26.0
Ave. AQY	11.4 ± 0.3	15.6 ± 0.7	27.0 ± 1.0

Reaction conditions: 50 ml of CH_3OH, 200 mg of ZIS-40, 2 bar of 5 vol% CO/Ar, 365 nm Xenon lamp (15 A).

Table S3. Summary of reported photocatalysts for EG production via methanol C−H bond scission.

Entry	Photocatalysts	Light source	EG selectivity (%)	AQY
1[10]	cis-$Rh_2Cl_2(CO)_2(dpm)_2$	High-pressure Hg lamp	59	N. M.[a]
2[11]	Colloidal ZnS	High-pressure Hg lamp	75	N. M.
3[12]	Hg	Low-pressure Hg lamp (254 nm)	97	34%
4[13]	MoS_2/CdS	300 W Xe lamp	90	5.2% (450 nm) 6.1% (380 nm)
5[14]	CoP/$Zn_2In_2S_5$	300 W Xe lamp or AM 1.5	90	3.0% (380 nm)[b]
6[15]	N-Ta_2O_5	300 W Xe lamp	71	N. M.
7[c]	In/ZIS-40	LEDs (365 ± 10 nm)	84	15.6% (365 nm)

[a] N. M. means not mentioned. [b] Estimated from the relative formation rate of EG since the same apparatus was used.
[c] This work.

Table S4. ICP-OES results of In/ZnS, Bi/ZnS and Cd/ZnS.

Photocatalyst	Metal content (wt%)
In/ZnS	0.24
Bi/ZnS	1.65
Cd/ZnS	0.95

Table S5. Calculated numbers of charge transfer between metals NPs and $ZnIn_2S_4$/ZnS.

$ZnIn_2S_4$		ZnS	
System	Average electron loss per atom (e^-)[a]	System	Average electron loss per atom (e^-)[a]
In	0.091	In	0.503
Pt	−0.006	Cd	0.347
		Bi	0.426
		Pt	−0.054
		Cu	0.008
		Ru	0.170

[a] Negative value means acquiring electrons.

Supplementary Figures

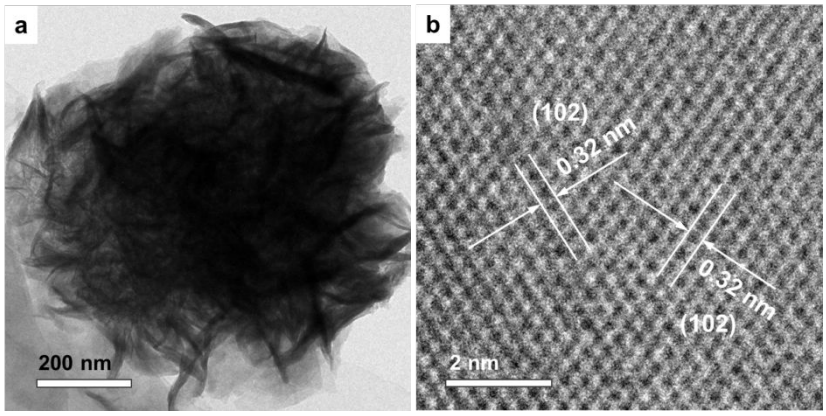

Figure S1. Representative TEM images of pristine $ZnIn_2S_4$. a. TEM image of $ZnIn_2S_4$, showing nanoflower shape constituted by sheet like wrinkles. **b**, High-resolution TEM (HRTEM) image of $ZnIn_2S_4$. The lattice fringes of 0.32 nm correspond to the (102) interplanar distance of hexagonal $ZnIn_2S_4$.[16]

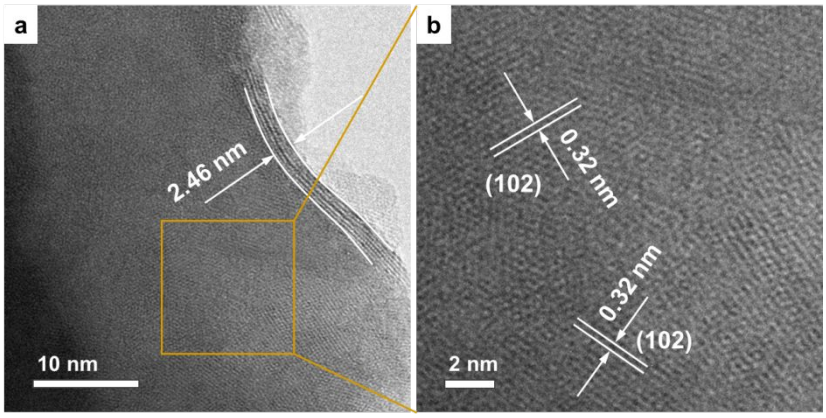

Figure S2. TEM images of the local structure of an indium nanoparticle of $In/ZnIn_2S_4$ sample. a, TEM image of an indium nanoparticle wrapped by a unit cell of $ZnIn_2S_4$. **b**, HRTEM of an indium nanoparticle, showing the lattice fringe corresponding to the (102) interplanar distance of $ZnIn_2S_4$.

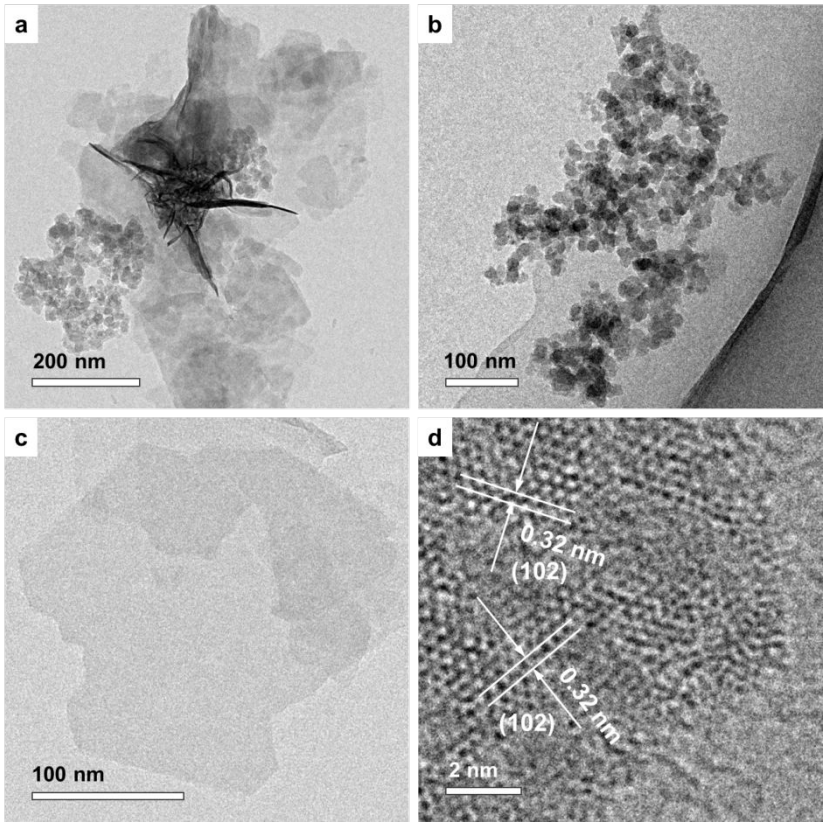

Figure S3. Representative TEM images of pristine ZIS-40 catalyst. a, **b** and **c** TEM images of ZIS-40 catalysts, showing ZIS-40 catalyst constituted by SiO_2 nanoparticles and ZIS nanosheets, either presented separately or in aggregation. **d**, HRTEM image of ZIS nanosheets, showing lattice fringes corresponding to (102) interplanar distance.[17]

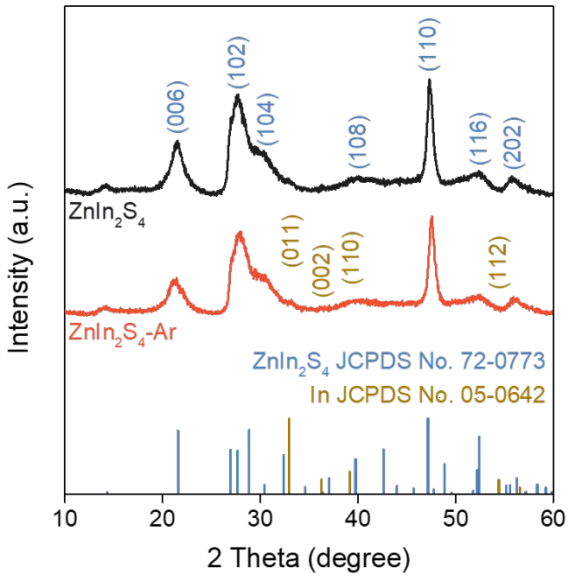

Figure S4. XRD patterns of pristine $ZnIn_2S_4$ and $ZnIn_2S_4$ after use in Ar.

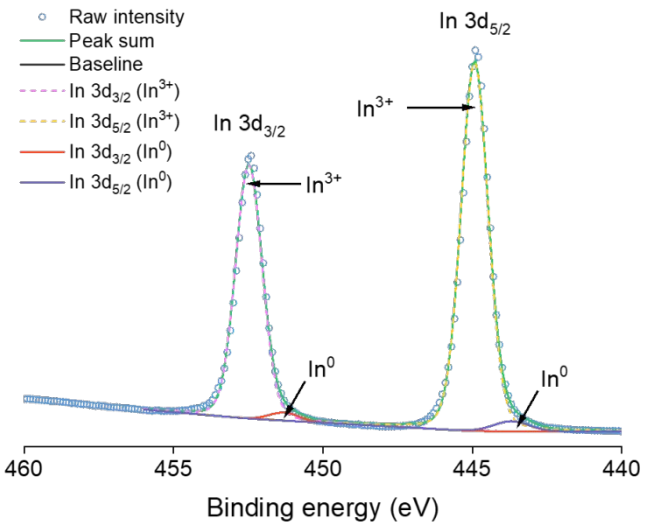

Figure S5. XPS of In/$ZnIn_2S_4$ after deconvolution. The content of metallic indium is about 3.2 mol%. The binding energy of In^0 and In^{3+} refers to In^0 in the literatures and In^{3+} of fresh $ZnIn_2S_4$, respectively.[18-19]

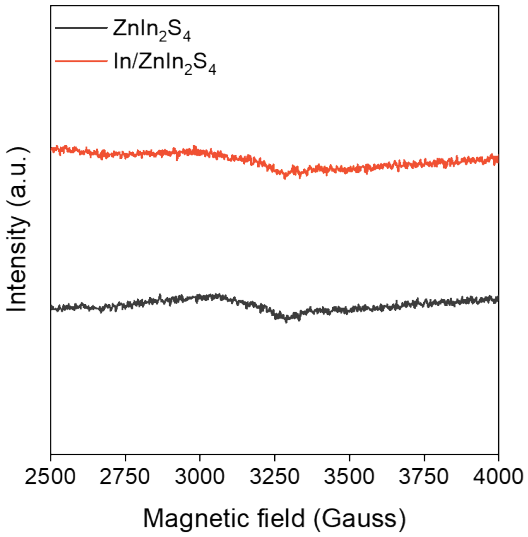

Figure S6. EPR of $ZnIn_2S_4$ and In/$ZnIn_2S_4$ recorded at 77 K. The weak signals are derived from the quartz tubes used to hold the samples.

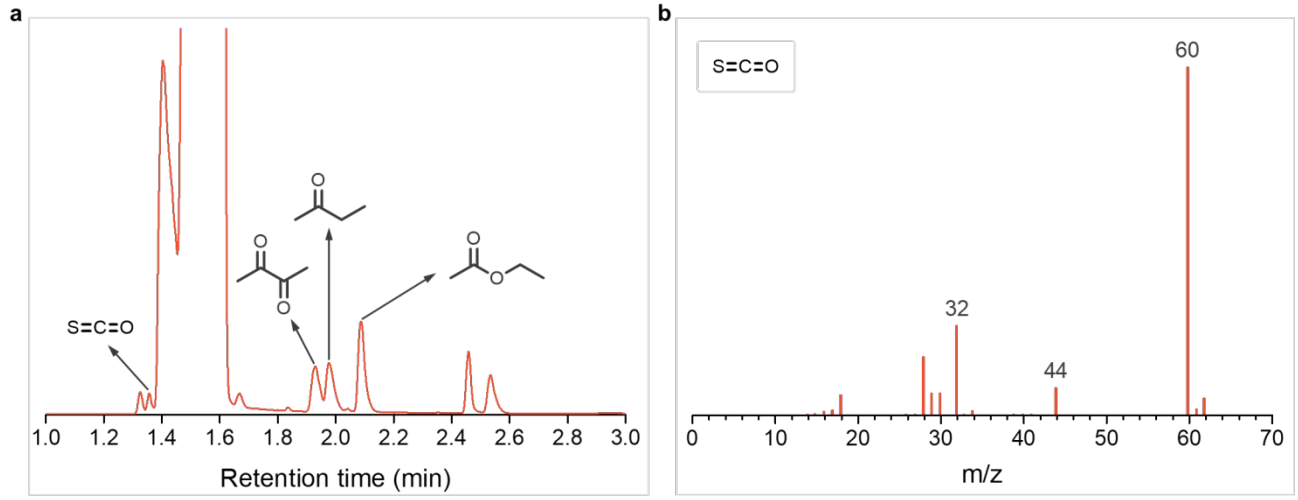

Figure S7. GC-Mass spectrometry detection of SCO molecule with ethanol as substrate. (a) Representative gas chromatogram of products in photocatalytic dehydrocoupling of ethanol. **(b)** Mass spectrogram of the substance with the retention time of 1.36 min. Reaction conditions: 1.5 ml of ethanol, 10 mg of $ZnIn_2S_4$, 2 bar of 5 vol% CO/Ar, 18 W LEDs (365 nm), 6 h. Because the retention time of methanol overlaps with S=C=O, ethanol was used instead of methanol to detect the formation of SCO.

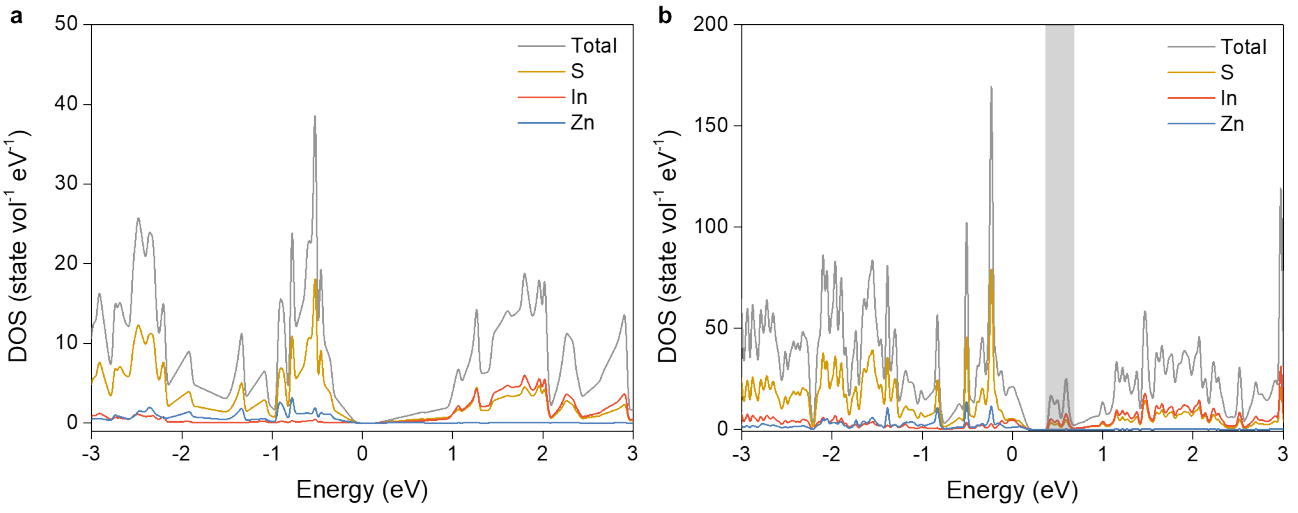

Figure S8. Calculated density of states (DOS) of $ZnIn_2S_4$ (a) and In/$ZnIn_2S_4$ (b).

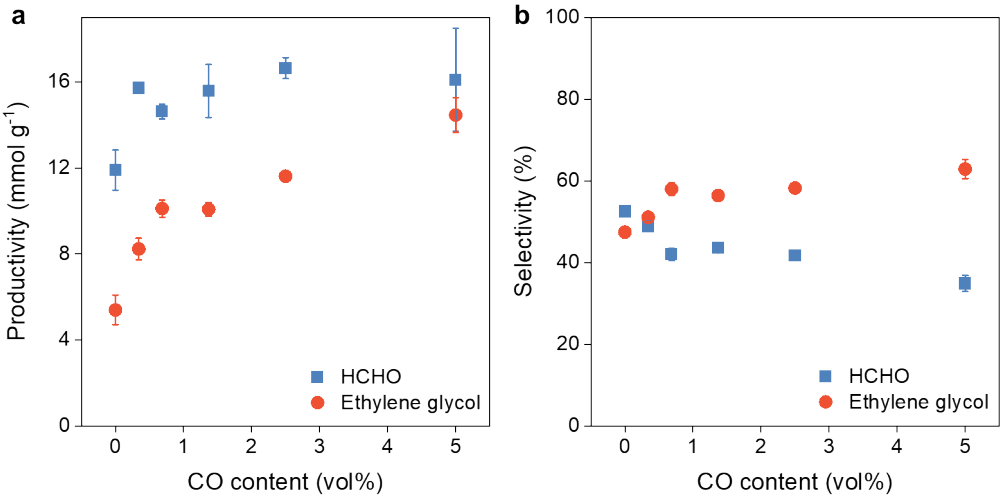

Figure S9. Influence of CO content on the photocatalytic DMEG. Influence of CO content on the productivity **(a)** and **(b)** selectivity of HCHO and EG.

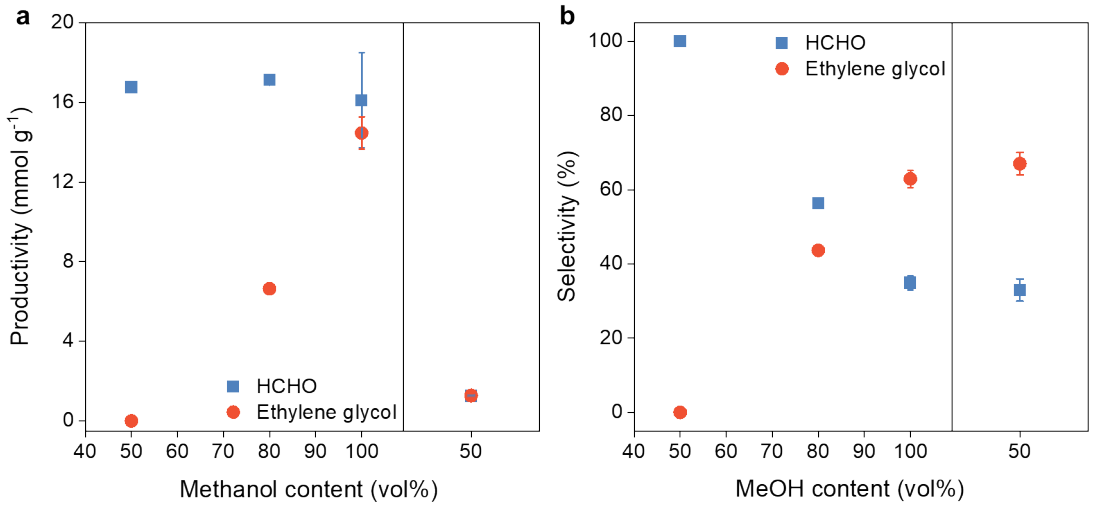

Figure S10. Influence of methanol content on the photocatalytic DMEG. Influence of methanol content on the productivity **(a)** and selectivity **(b)** of HCHO and EG. For both figures, the left and right panels represent the reaction results of methanol-water and methanol-MeCN, respectively.

When reducing methanol content (the residual is water), the productivity and selectivity of EG decrease dramatically. Particularly, when methanol content is 50 vol%, methanol is converted to exclusively HCHO. The productivity of HCHO nearly remains unchanged along with the decrease of methanol content. These results could be tentatively rationalized by the inability to form In^0 NPs. When water is in a large volume fraction, In NPs would be re-oxidized back to In^{3+} since In NPs are highly active. This hypothesis could be supported by the reaction results of the methanol-MeCN mixture. Although the methanol-MeCN mixture is converted to HCHO and EG with far lower productivity than that of pure methanol due to a lower concentration of methanol, the selectivity of EG (67%) is comparable to that of pure methanol (63%). The above results support that formation of In^0 NPs improves the selectivity of EG.

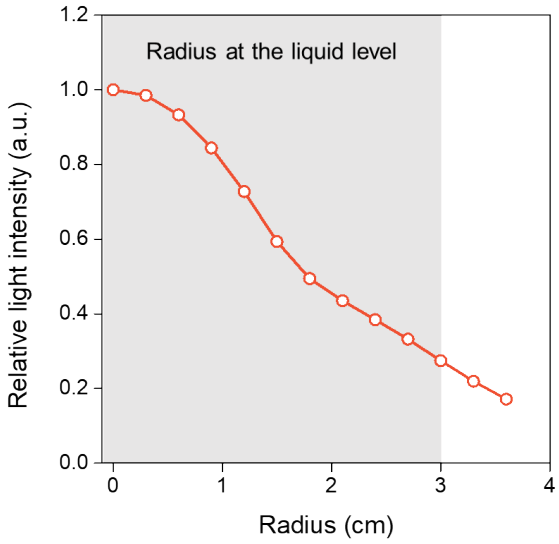

Figure S11. Measured radial distribution of light intensity of 365 nm LEDs (103 W, 365 ± 10 nm). The radius at the liquid level of the reaction solution was 3.0 cm.

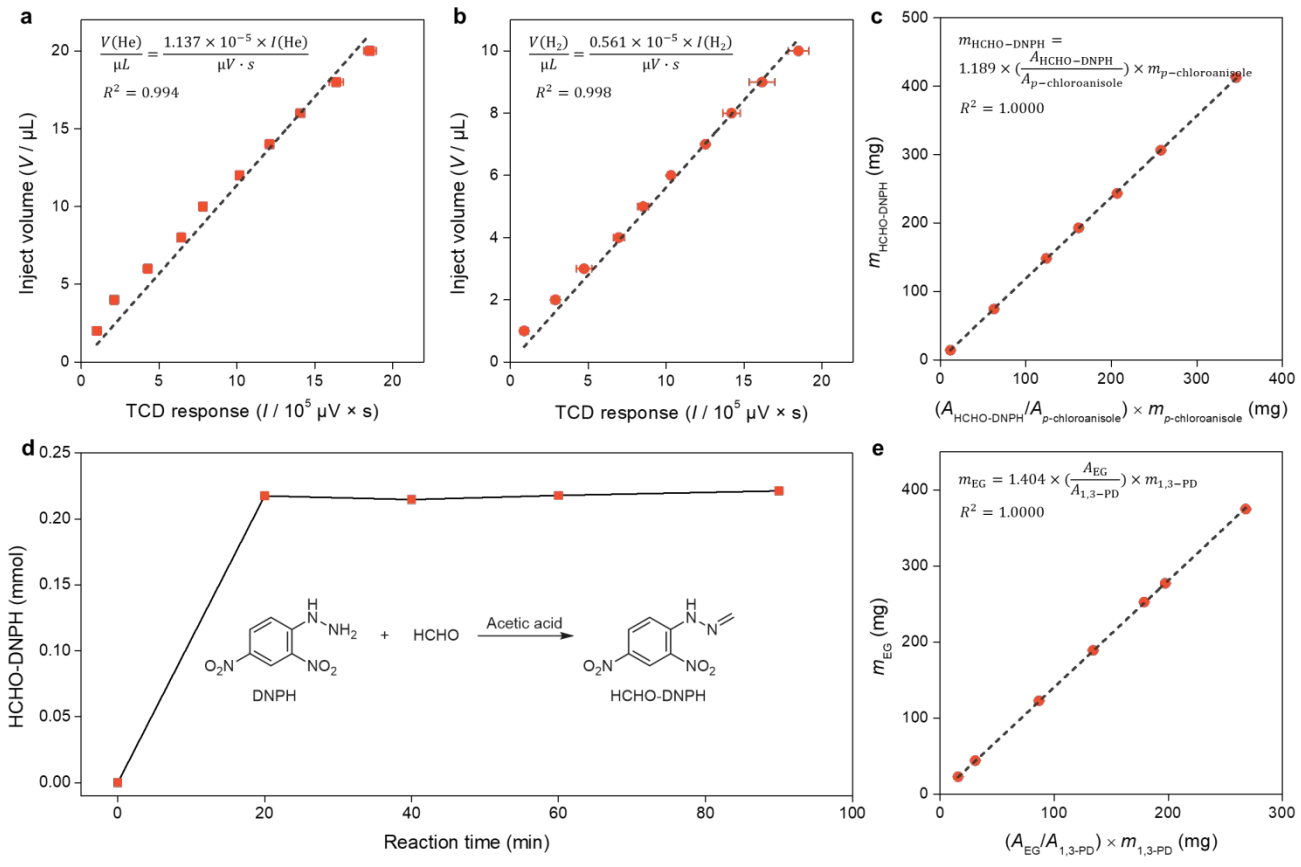

Figure S12. Calibration results of products. Calibration curves of He **(a)** and H_2 **(b)**. Calibration curves of HCHO-DNPH **(c)** along with the time profile of the reactions between HCHO and DNPH, the derivatization reagent **(d)**. **e**, Calibration curves of EG with 1,3-PD as the internal standard.

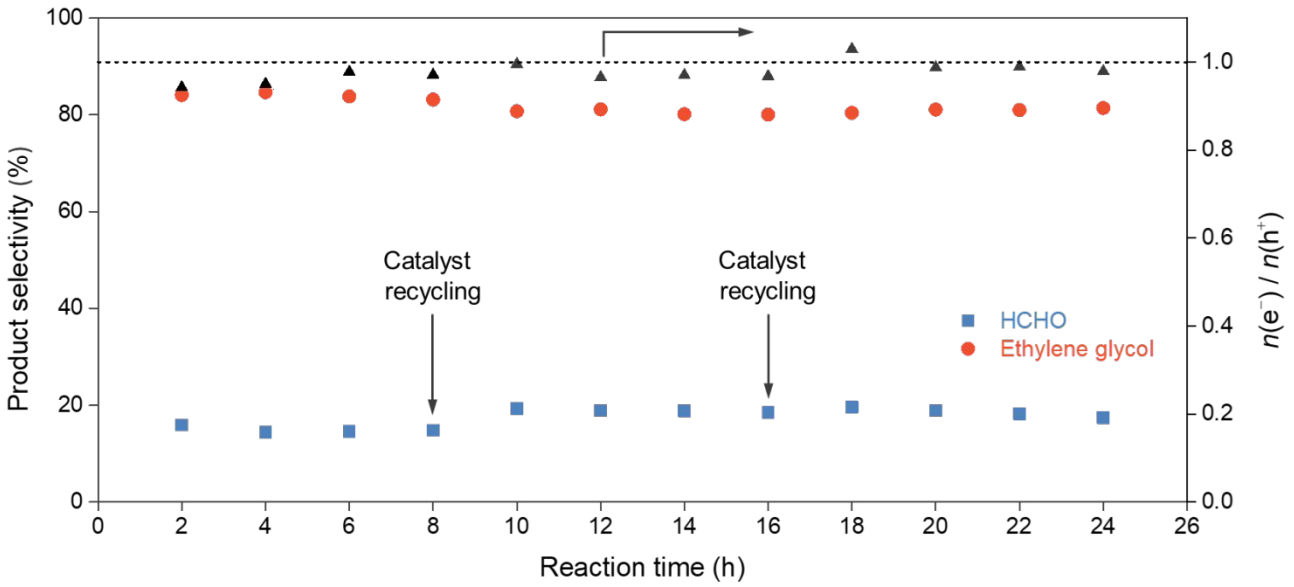

Figure S13. Product selectivity and n(e^-)/n(h^+) values in catalyst recycling experiments conducted with In/ZIS-40 catalyst. Reaction conditions: 50 ml of MeOH, 100 mg of ZIS-40, 2 bar of 5 vol% CO/Ar, 103 W LEDs (365 nm).

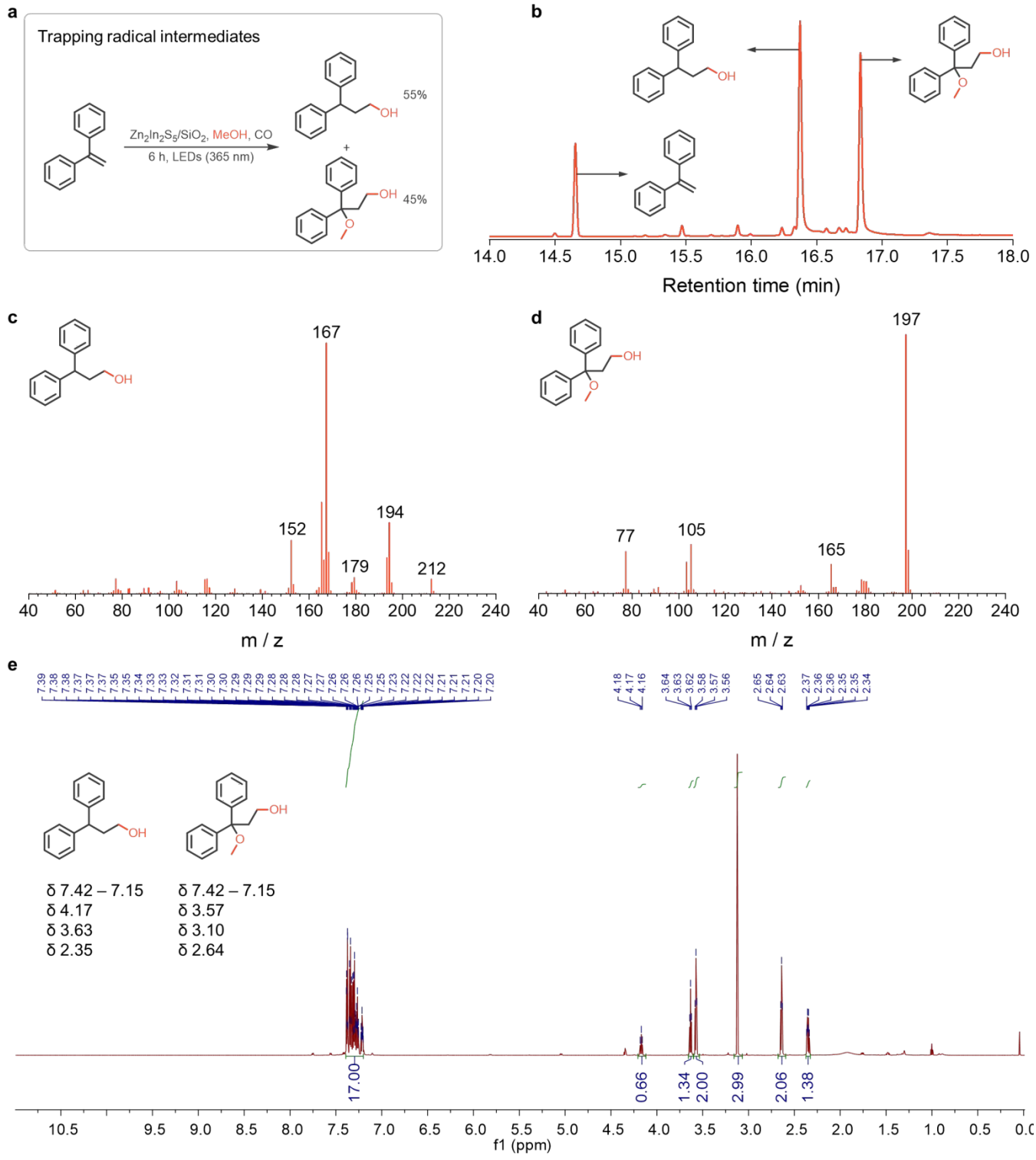

Figure S14. Capturing radical intermediates by 1,1-diphenylethylene in photocatalytic MDEG. a, Reaction formulas of 1,1-diphenylethylene with radical intermediates. **b**, Representative GC chromatogram. Mass spectrograms of substances at retention time of 16.4 **(c)** and 16.9 min **(d)**, respectively. **e**, ^{1}H NMR of the radical capturing products after purification. ^{1}H NMR (700 MHz, $CDCl_3$) δ 7.42 – 7.15 (m, 17.00 H), 4.17 (t, J = 7.9 Hz, 0.66 H), 3.63 (t, J = 6.5 Hz, 1.34 H), 3.57 (t, J = 6.3 Hz, 2.00 H), 3.10 (d, J = 33.5 Hz, 2.99 H), 2.64 (t, J = 6.3 Hz, 2.06 H), 2.35 (dt, J = 7.9, 6.5 Hz, 1.38 H).

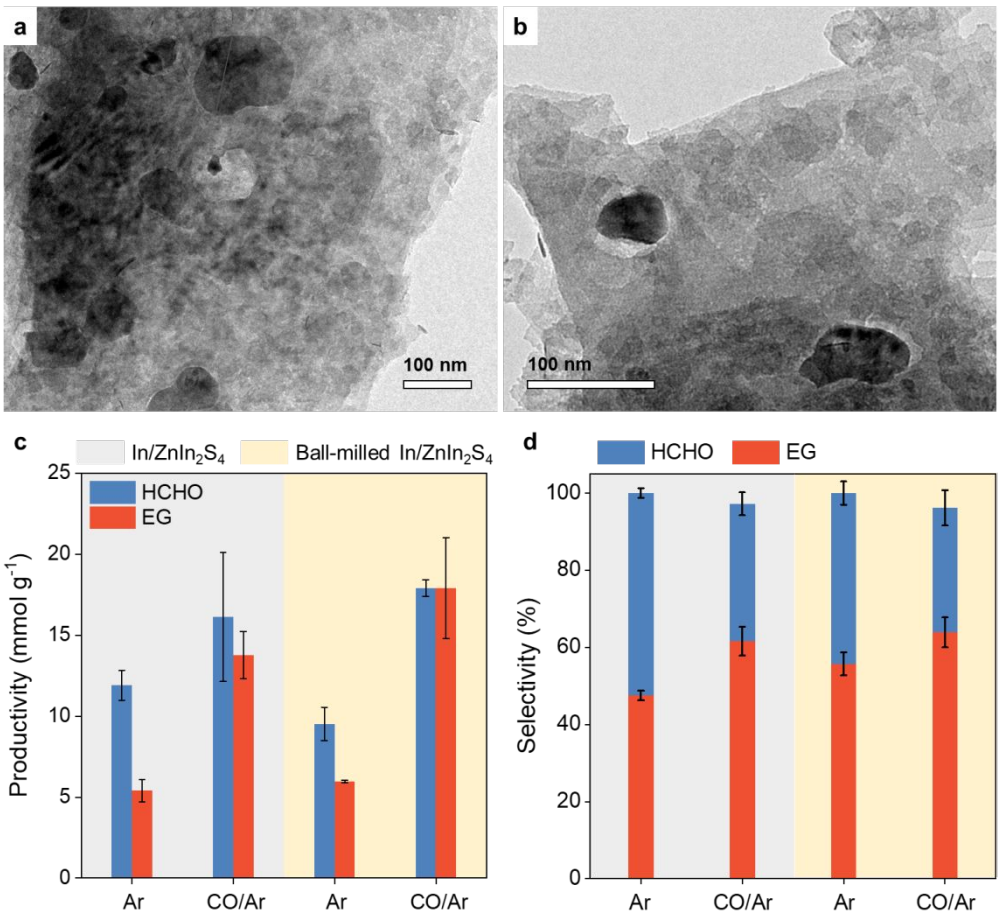

Figure S15. TEM images of ball-milled In/$ZnIn_2S_4$ and the reaction results of photocatalytic DMEG by the ball-milled In/$ZnIn_2S_4$. a and **b**, TEM images of ball-milled In/$ZnIn_2S_4$, showing In NPs from dozens of nanometers to about 150 nm. Productivities **(c)** and selectivity **(d)** of HCHO and EG in photocatalytic DMEG by In/$ZnIn_2S_4$ (in gray) and ball-milled In/$ZnIn_2S_4$ (in yellow). Standard reaction conditions: 1.5 ml of methanol, 10 mg of catalyst, 2 bar of 5 vol% CO/Ar, 18 W LEDs (365 nm), 6 h.

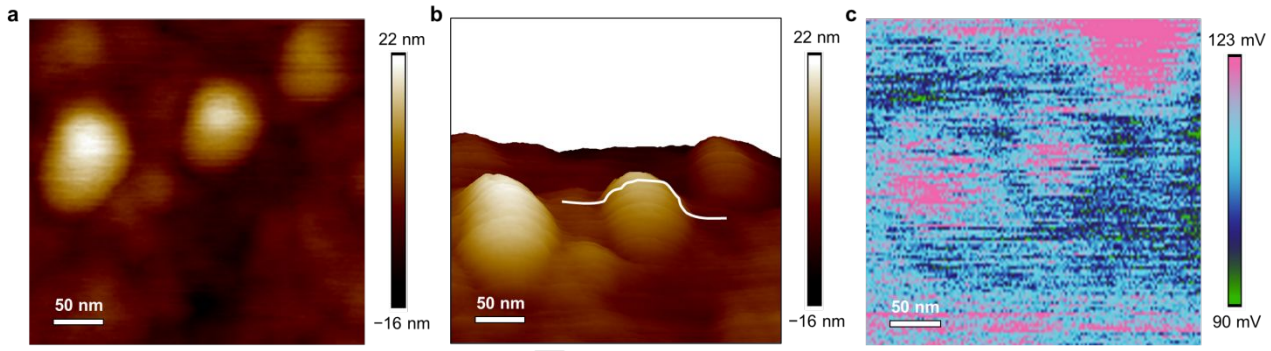

Figure S16. Kelvin probe force microscope (KPFM) of In/$ZnIn_2S_4$ catalyst. AFM height image **(a)** and three-dimensional AFM height image **(b**) of In/$ZnIn_2S_4$ catalyst, showing clearly well dispersed In NPs with sizes from about 30 to 80 nm. **c**, CPD of In/$ZnIn_2S_4$ catalyst, showing a larger CPD in the region of In NPs, indicating a smaller work function of In NPs than the $ZnIn_2S_4$ substrate.

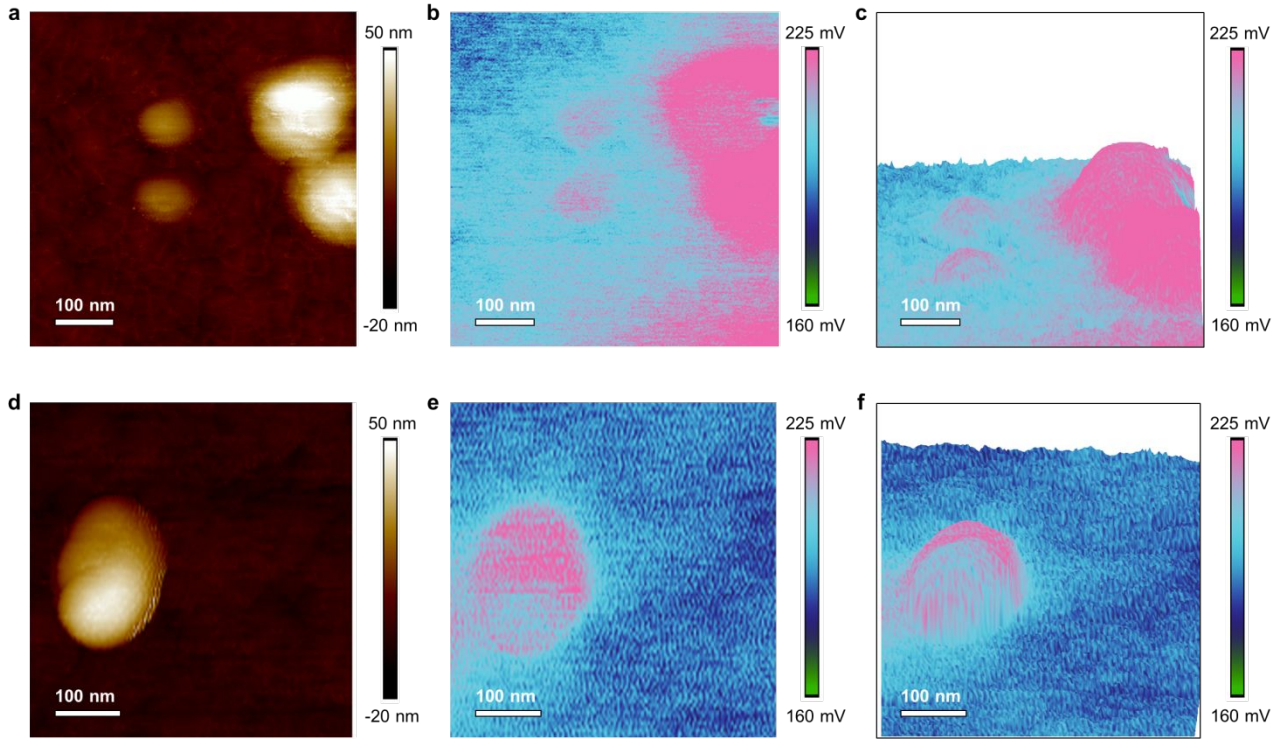

Figure S17. Confirming a lower work function of In NPs than the $ZnIn_2S_4$ substrate by Kelvin probe force microscope (KPFM). AFM height image **(a)** of In/$ZnIn_2S_4$ catalyst, showing clearly well dispersed In NPs with sizes from 80 to 160 nm. **b** and **c**, CPD of In/$ZnIn_2S_4$ catalyst, showing a larger CPD in the region of In NPs. AFM height image **(d)** of In/$ZnIn_2S_4$ catalyst, showing two In NPs with sizes about from 170 nm. **e** and **f**, CPD of In/$ZnIn_2S_4$ catalyst, showing a larger CPD in the region of In NPs.

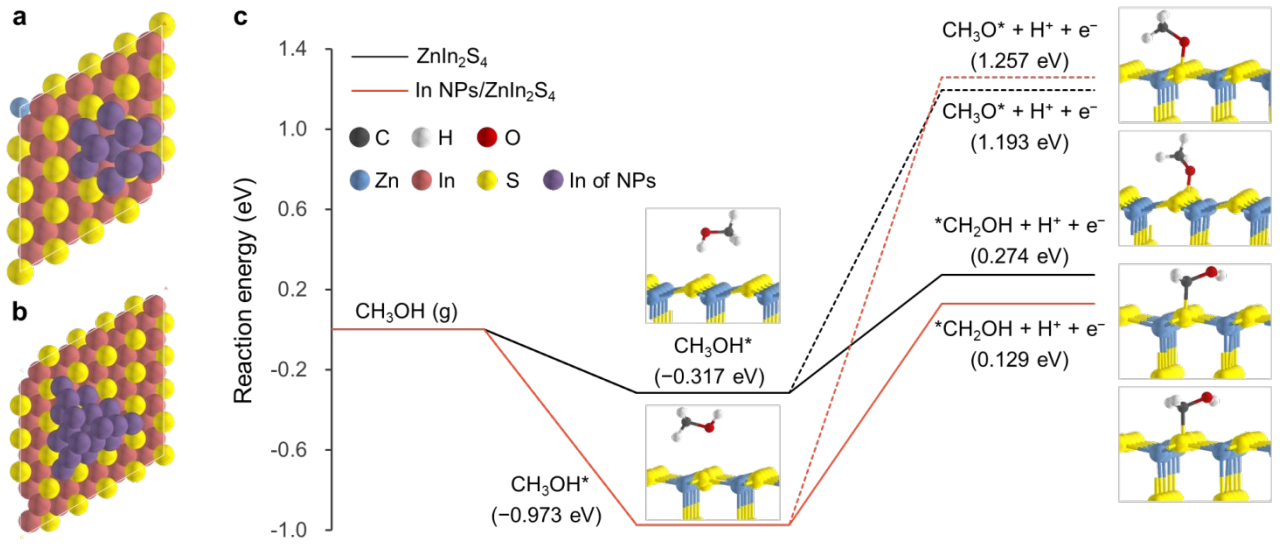

Figure S18. DFT Calculation results by using a $ZnIn_2S_4$ (5×5×0.5) surface model. Top view of In/$ZnIn_2S_4$ by using the $ZnIn_2S_4$ (4×4×0.5) surface model **(a)** and $ZnIn_2S_4$ (5×5×0.5) surface model **(b)**. **c**, Calculation results of C−H and O−H bond scission over $ZnIn_2S_4$ and In/$ZnIn_2S_4$ using a $ZnIn_2S_4$ (5×5×0.5) surface model.

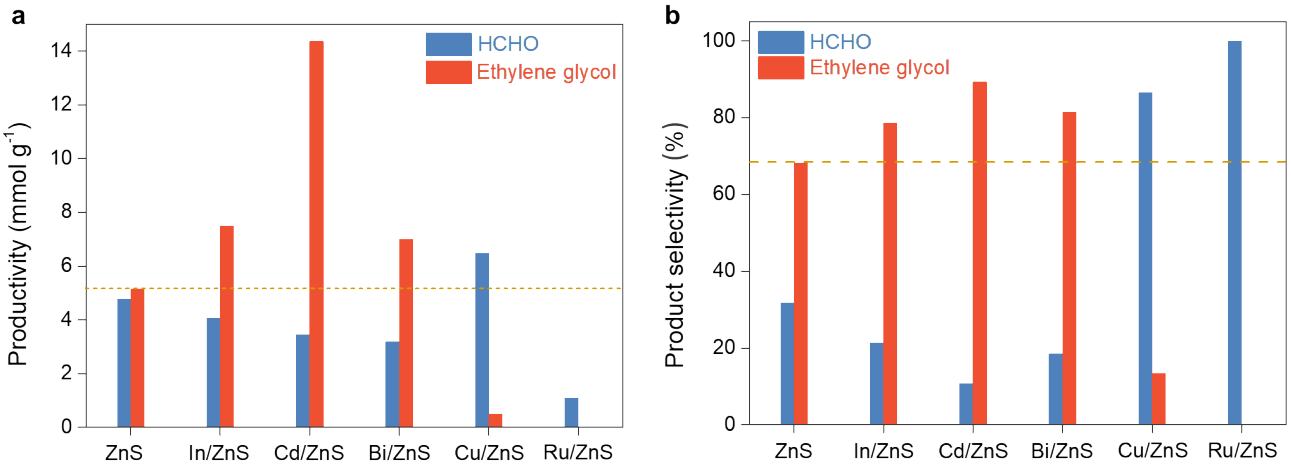

Figure S19. Reaction results of photocatalytic MDEG over ZnS supported with metal NPs. Productivity **(a)** and selectivity **(b)** of HCHO and EG over ZnS supported with metal NPs (M^0 NPs/ZnS). Reaction conditions: 1.4 ml of MeOH, 0.1 ml of diethylene glycol, 10 mg of M^0 NPs/ZnS, 2 bar of 5 vol% CO/Ar, 18 W LEDs (365 nm), 6 h. The contents of In, Cd and Bi were determined to be 0.95 wt%, 1.65 wt% and 0.24 wt%, respectively by inductively coupled plasma optical emission spectrometer.

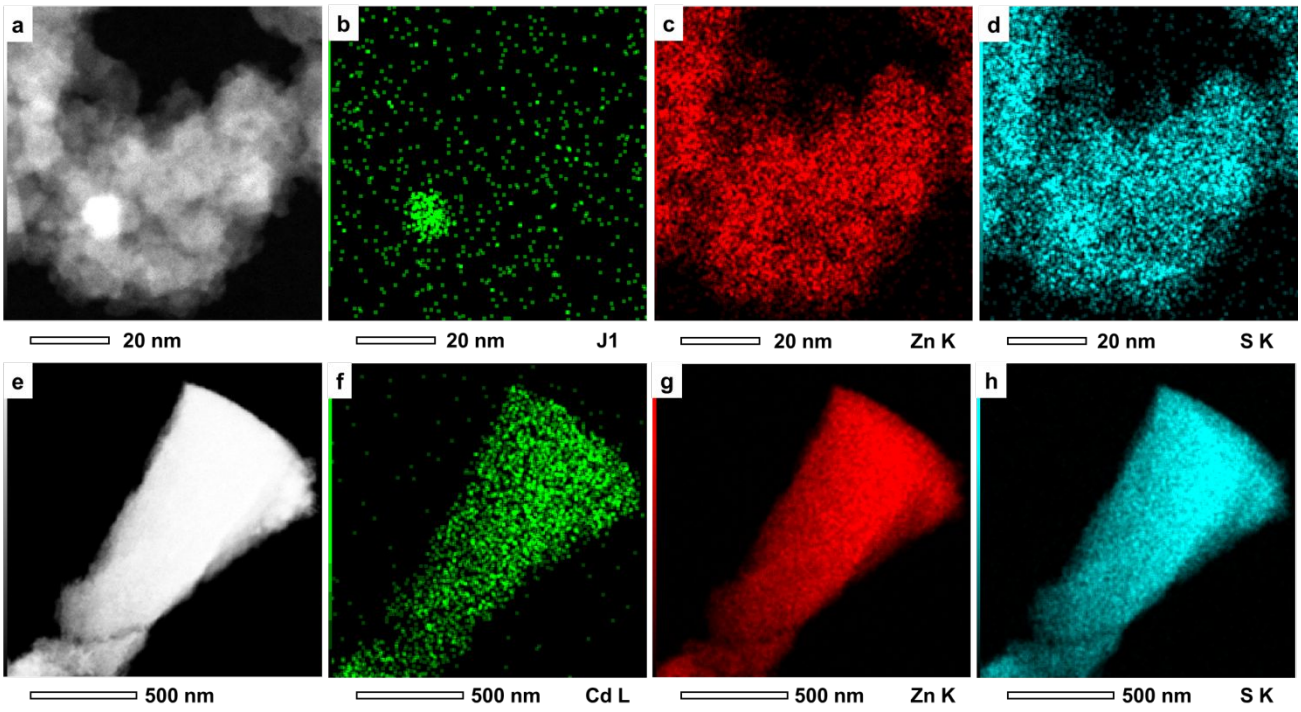

Figure S20. EDX mappings of Bi/ZnS and Cd/ZnS. a, STEM image of Bi/ZnS. EDX mappings of J1 edge **(b)**, Zn K edge **(c)** and S K edge **(d)**. **e**, STEM image of Cd/ZnS. EDX mappings of Cd L edge **(f)**, Zn K edge **(g)** and S K edge **(h)**.

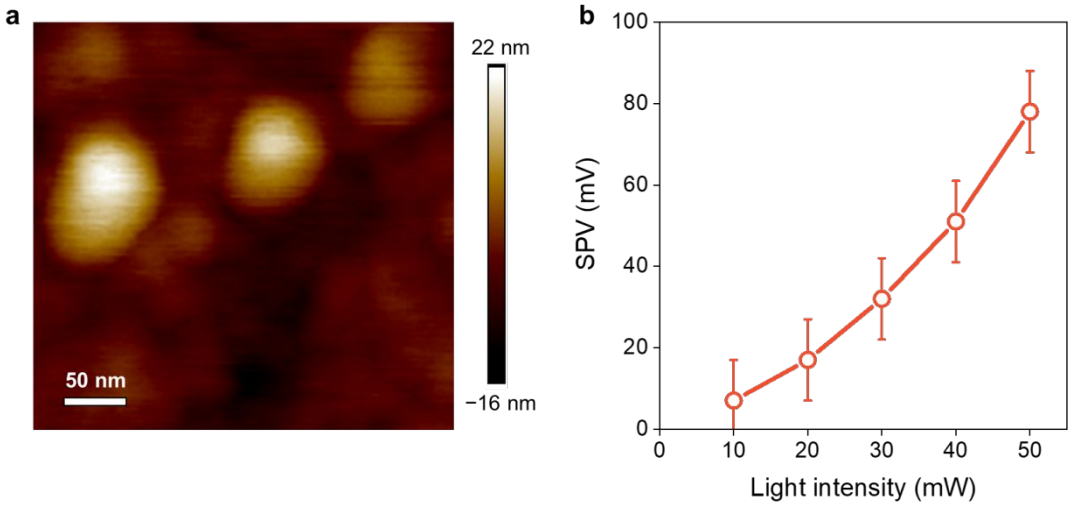

Figure S21. Surface photovoltage microscopy (SPVM) measurement of In/$ZnIn_2S_4$ catalyst. a, Light-excitation KPFM image of In/$ZnIn_2S_4$ catalyst under irradiation of 405 nm laser. **b**, Relationship between SPV values and light intensities measured on In NPs.

References

1. Kind, C.; Feldmann, C. One-Pot Synthesis of In^0 Nanoparticles with Tuned Particle Size and High Oxidation Stability. *Chem. Mater.* **2011**, *23*, 4982–4987.

2. Jang, J. S.; Joshi, U. A.; Lee, J. S. Solvothermal Synthesis of CdS Nanowires for Photocatalytic Hydrogen and Electricity Production. *J. Phys. Chem. C* **2007**, *111*, 13280–13287.

3. Kresse, G.; Furthmiiller, J. Efficiency of ab-Initio Total Energy Calculations for Metals and Semiconductors Using a Plane-Wave Basis Set. *Comp. Mater. Sci.* **1996**, *6*, 15–50.

4. Kresse, G.; Furthmu¨ller, J. Efficient Iterative Schemes for ab Initio Total-Energy Calculations Using a Plane-Wave Basis Set. *Phys. Rev. B* **1996**, *54*, 11169–11186.

5. Perdew, J. P.; Burke, K.; Ernzerhof, M. Generalized Gradient Approximation Made Simple. *Phys. Rev. B* **1996**, *77*, 3865–3868.

6. Blöchl, P. E. Projector Augmented-Wave Method. *Phys. Rev. B* **1994**, *50*, 17953–17979.

7. Kresse, G.; Joubert, D. From Ultrasoft Pseudopotentials to the Projector Augmented-Wave Method. *Phys. Rev. B* **1999**, *59*, 1758–1775.

8. Grimme, S.; Antony, J.; Ehrlich, S.; Krieg, H. A Consistent and Accurate ab Initio Parametrization of Density Functional Dispersion Correction (DFT-D) for the 94 Elements H-Pu. *J. Chem. Phys.* **2010**, *132*, 154104.

9. Donika, F. G.; Kiosse, G. A.; Radautsan, S. I.; Semiletov, S. A.; Mustya, I. G. CrystalStructure of the Two Pack Polytypic Form $ZnIn_2S_4$ (II)B. *Kristallografiya* **1972**, *17*, 663–665.

10. Yamamoto, H.; Shinoda, S.; Salto, Y. Photocatalytic Dehydrogenation of Methanol in the Liquid Phase with cis-$Rh_2Cl_2(CO)_2(dpm)_2$ and $Pd_2Cl_2(dpm)_2$ Complex Catalysis. *J. Mol. Catal.* **1985**, *30*, 259–266.

11. Yanagida, S.; Azuma, T.; Kawakami, H.; Kizumoto, H.; Sakurai, H. Photocatalytic Carbon-Carbon Bond Formation with Concurrent Hydrogen Evolution on Colloidal Zinc Sulphide. *J. Chem. Soc. Chem. Commun.* **1984**, *1*, 21–22.

12. Brown, S. H.; Crabtree, R. H. Making Mercury-Photosensitized Dehydrodimerization into an Organic Synthetic Method: Vapor Pressure Selectivity and the Behavior of Functionalized Substrates. *J. Am. Chem. Soc.* **1989**, *111*, 2935–2946.

13. Xie, S.; Shen, Z.; Deng, J.; Guo, P.; Zhang, Q.; Zhang, H.; Ma, C.; Jiang, Z.; Cheng, J.; Deng, D.; Wang, Y. Visible Light-Driven C−H Activation and C−C Coupling of Methanol into Ethylene Glycol. *Nat. Commun.*

2018, *9*, 1181.

14. Zhang, H.; Xie, S.; Hu, J.; Wu, X.; Zhang, Q.; Cheng, J.; Wang, Y. C−H Activations of Methanol and Ethanol and C−C Couplings into Diols by Zinc-Indium-Sulfide under Visible Light. *Chem. Commun.* **2020**, *56*, 1776−1779.

15. Wang, L.; Du, D.; Zhang, B.; Xie, S.; Zhang, Q.; Wang, H.; Wang, Y. Solar Energy-Driven C−H Activation of Methanol for Direct C−C Coupling to Ethylene Glycol with High Stability by Nitrogen Doped Tantalum Oxide. *Chin. J. Catal.* **2021**, *42*, 1459–1467.

16. Donika, F. G.; Radautsan, S. I.; Mustya, I. G.; Kiosse, G. A.; Semiletov, S. A.; Donika, T. V. Crystal Structure of the Double-Pack Polytype $ZnIn_2S_4$ (II)a, and More Careful Determination of the Structure of the Triple-Pack Polytype $ZnIn_2S_4$ (III)a. *Sov. Phys. Crystallogr.* **1971**, *15*, 698–700.

17. Wang, S.; Guan, B. Y.; Lou, X. W. D. Construction of $ZnIn_2S_4$-In_2O_3 Hierarchical Tubular Heterostructures for Efficient CO_2 Photoreduction. *J. Am. Chem. Soc.* **2018**, *140*, 5037–5040.

18. Brojerdi, G.; Tyuliev, G.; Fargues, D.; Eddrief, M.; Balkanski, M. Ion Beam Modification of InSe Surfaces. *Surf. Interface Anal.* **1997**, *25*, 111–118.

19. Detweiler, Z. M.; Wulfsberg, S. M.; Frith, M. G.; Bocarsly, A. B.; Bernasek, S. L. The oxidation and surface speciation of indium and indium oxides exposed to atmospheric oxidants. *Surf. Sci.* **2016**, *648*, 188–195.